Three dimensional nonlinear simulations of edge localized modes on the EAST tokamak using BOUT++ code

Z. X. Liu, X. Q. Xu, X. Gao, T. Y. Xia, I. Joseph, W. H. Meyer, S. C. Liu, G. S. Xu, L. M. Shao, S. Y. Ding, G. Q. Li, and J. G. Li

Citation: Physics of Plasmas **21**, 090705 (2014); doi: 10.1063/1.4895799
View online: http://dx.doi.org/10.1063/1.4895799
View Table of Contents: http://scitation.aip.org/content/aip/journal/pop/21/9?ver=pdfcov
Published by the AIP Publishing

Three dimensional nonlinear simulations of edge localized modes on the EAST tokamak using BOUT++ code

Z. X. Liu,[1,2,a)] X. Q. Xu,[2] X. Gao,[1] T. Y. Xia,[1,2] I. Joseph,[2] W. H. Meyer,[2] S. C. Liu,[1,2] G. S. Xu,[1] L. M. Shao,[1] S. Y. Ding,[1,2] G. Q. Li,[1] and J. G. Li[1]
[1]*Institute of Plasma Physics, Chinese Academy of Sciences, Hefei 230031, China*
[2]*Lawrence Livermore National Laboratory, Livermore, California 94550, USA*

(Received 10 February 2014; accepted 26 August 2014; published online 12 September 2014)

Experimental measurements of edge localized modes (ELMs) observed on the EAST experiment are compared to linear and nonlinear theoretical simulations of peeling-ballooning modes using the BOUT++ code. Simulations predict that the dominant toroidal mode number of the ELM instability becomes larger for lower current, which is consistent with the mode structure captured with visible light using an optical CCD camera. The poloidal mode number of the simulated pressure perturbation shows good agreement with the filamentary structure observed by the camera. The nonlinear simulation is also consistent with the experimentally measured energy loss during an ELM crash and with the radial speed of ELM effluxes measured using a gas puffing imaging diagnostic. © *2014 AIP Publishing LLC*. [http://dx.doi.org/10.1063/1.4895799]

High-performance (H-mode) discharges[1] with an edge transport barrier are the current baseline operating scenario for ITER. The steep pressure gradients and associated bootstrap current destabilize magneto-hydrodynamic peeling-ballooning modes and generate repetitive unstable edge localized mode (ELM) events,[2] which lead to eruptions of filamentary structures from the plasma. The energy released during the ELMs is deposited on the divertor and may quickly erode the material surfaces of divertors in future devices. Understanding the structure of peeling-ballooning modes has been developed using linear codes such as ELITE[3] and GATO,[4] and nonlinear simulations have been performed with NIMROD[5] and JOREK.[6] This letter describes the first comparison between measurements of ELMs on the EAST tokamak and nonlinear simulations of ELM physics using the BOUT++ code.[7] Simulation predictions are compared to the poloidal mode structure of the ELM measured using a visible camera, the total energy losses during the ELM measured from equilibrium reconstruction, and the speed of the ELM effluxes measured with a gas puff imaging diagnostic (GPI).

The BOUT++ simulations are based on the peeling-ballooning model with non-ideal physics effects such as the diamagnetic drift, $E \times B$ drift, resistivity, and anomalous electron viscosity. A minimum set of nonlinear equations for perturbations of the magnetic flux $A_{\|}$, electric potential ϕ, and pressure P can be extracted from the complete set of BOUT two fluid equations[7] with the additional effects of hyper-resistivity[8] and parallel viscosity. The BOUT++ three field model,[9,10] which evolves vorticity, pressure, and parallel vector potential, has been used to simulate peeling-ballooning modes on DIII-D, C-mod, K-STAR, and EAST. The three-field equations used here are given explicitly in Ref. 11. An important assumption of the model is that the axisymmetric electric and ion diamagnetic drifts cancel to provide radial ion force balance. The diamagnetic effects stabilize the ELM instabilities at large toroidal mode number.[12]

The filamentary structure of an ELM instability can be clearly identified during the initial phases of a simulation. Images of electron temperature fluctuations near the separatrix were first observed using the electron cyclotron emission (ECE) imaging system on K-STAR in 2012, which capture the filament structure clearly during the initial phase.[13] However, the time of the initial phase is very short and the electron temperature is too high to generate visible radiation observable by a typical CCD camera. Thus, it is difficult for most tokamaks to view the ELM structure directly from a CCD camera. The earliest observation of the filament structure of ELMs was obtained by a high-speed camera with a short (20 μs) exposure time on MAST in 2004. The structure was obtained at the start of an ELM, and ELM effluxes are observed radially up to 20 cm from the plasma edge,[14] where the filament becomes sufficiently cool to be observed. On EAST, a CCD camera facing a movable limiter has been used to image ELM filaments located below the outer midplane. The filamentary structures of an ELM instability cool down as they contact the movable limiter and, thus, become cool enough to emit visible radiation that is captured by the CCD camera.

Linear BOUT++ simulations predict that the dominant toroidal mode number of ELMs becomes larger for lower total plasma current.[11] To verify these simulation results, we varied the current in EAST plasma discharge #41019. This discharge was operated with a combination of ion cyclotron resonance frequency (ICRF) and lower hybrid wave (LHW) heating power. During the H-mode phase, the toroidal field is 2 T, the line-averaged density is $3.9 \times 10^{19}\,m^{-3}$, the electron temperature near the pedestal top is about 0.45 keV, P_{LHW} is 1 MW, and P_{ICRF} is 0.8 MW. The plasma current (I_p) is decreased rapidly from 400 kA at time 3100 ms to 300 kA within about 1500 ms. Filamentary structures, shown

a)Author to whom correspondence should be addressed. Electronic mail: zxliu316@ipp.ac.cn.

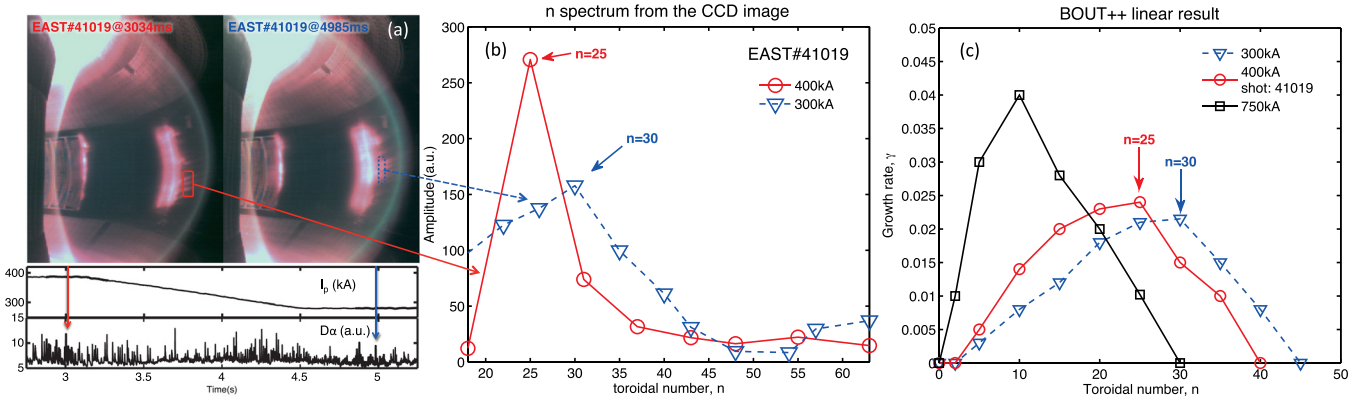

FIG. 1. (a) Filament structure captured by the CCD camera at time 3034 ms and time 4985 ms. The dashed line rectangular windows are selected for analysis of the poloidal wavenumber. (b) The toroidal mode # spectrum inferred from the CCD images. (c) Predicted linear growth rate vs. toroidal number for different plasma currents.

in Fig. 1(a), were observed using the CCD camera for the cases of $I_p = 400$ kA (time 3034 ms) and $I_p = 300$ kA. A comparison of the two images shows that the filaments for $I_p = 400$ kA (time 4089 ms) are obviously denser than for $I_p = 300$ kA. To obtain a quantitative result, the images are mapped to absolute spatial coordinates and a window, enclosed by the red and blue line rectangular boxes shown in Fig. 1(a), is selected for analysis. A Fourier transform along the vertical direction yields the poloidal mode number of the filament k_p. Assuming that the filaments are aligned with the magnetic field, the poloidal mode number is proportional to the toroidal mode number via $n = m/q = k_p R B_p / B_T$, where the safety factor q is related to the plasma current. The toroidal spectrum shown in Fig. 1(b) shows the amplitude peaks at $n = 25$ ($k_p = 104\,\mathrm{m}^{-1}$) for $I_p = 400$ kA and at $n = 30$ ($k_p = 150\,\mathrm{m}^{-1}$) for $I_p = 300$ kA. Although the experimental results are only $\pm 30\%$–50% accurate based on the half-width at half height of the measured peak, they are qualitatively consistent with the results of the previous linear simulations.[11]

Linear and nonlinear simulations based on the ELMy H-mode discharge #41019 were performed using the BOUT++ two fluid framework. Shot #41019 at 3034 ms did not have enough experimental data to construct a kinetic EFIT equilibrium reconstruction. Instead, we generated an equilibrium by modifying a kinetic EFIT reconstruction for a similar shot #33068 at 2900 ms using the Corsica transport code.[15] The original profiles for #33068 at 2900 ms are shown in Ref. 16. To generate an approximate "kinetic EFIT" for #41019, we scaled the pressure by the line-averaged density ($3.9 \times 10^{19}\,\mathrm{m}^{-3}$ in shot #41019 vs. $3.5 \times 10^{19}\,\mathrm{m}^{-3}$ in shot #33068) and scaled the total current I_p (400 kA in shot #41019 vs. 500 kA in shot #33068). Shot #41019 is a double-null discharge with $\mathrm{dR_{sep}} = 0.1$ at time = 3034 ms, which means that the configuration is closer to upper single-null. (Magnetic divertor balance is described by

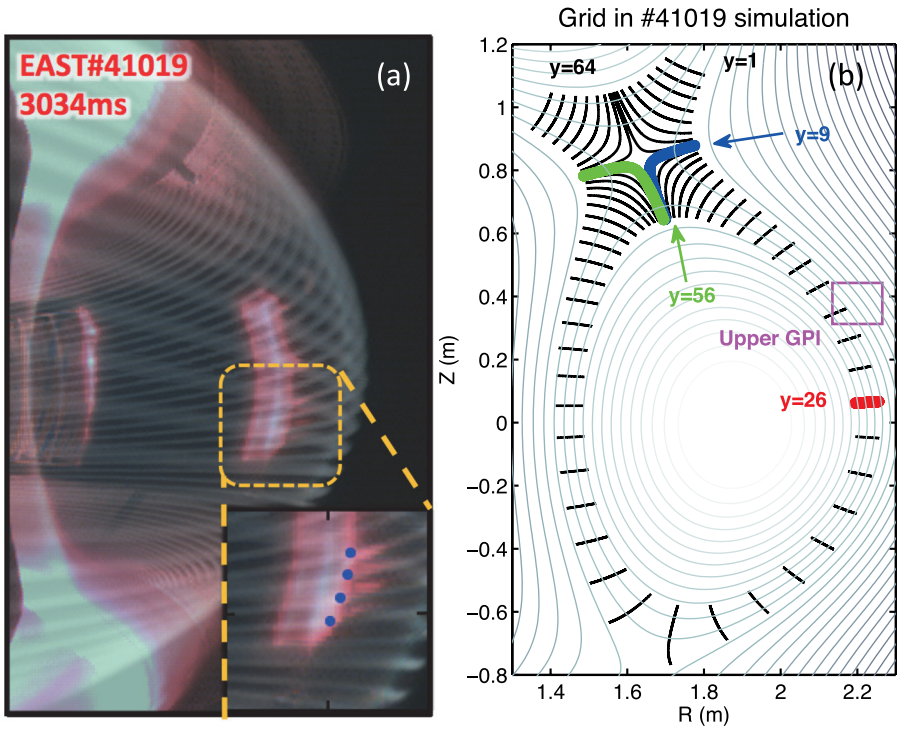

FIG. 2. (a) ELM pressure perturbations (a.u.) from the simulation as observed by a synthetic ray-tracing diagnostic (bright white lines). (b) Mesh used for the simulation: black lines show the poloidal (y) grid and blue lines show a subset of flux surfaces used for the radial (x) grid. The GPI observation window is marked as a pink rectangle.

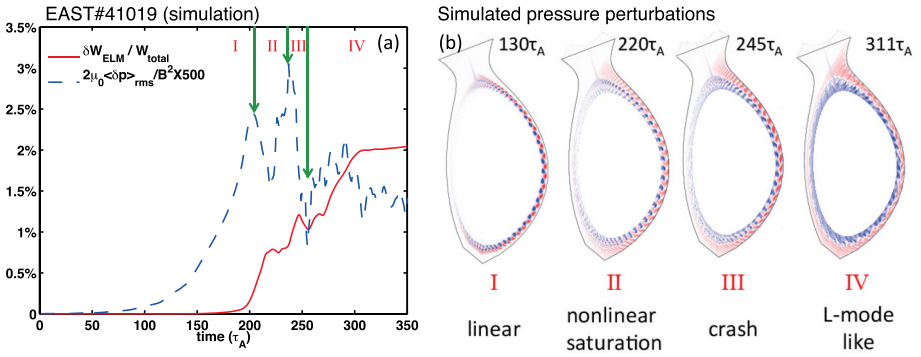

FIG. 3. Four phases of the ELM crash from the nonlinear simulation. (a) The normalized rms value of the pressure perturbation (dashed blue line) and the ELM loss (solid red line). (b) The pressure perturbations at different phases of the ELM crash.

dR_{sep}, the radial separation at the low-field side mid-plane between the flux surfaces connected to the upper and lower divertor X-points.) For simplicity, we choose the region to vary in normalized poloidal flux ψ from 0.8 to 1.02 to make the selected region single-null. The radial simulation dimension is about 4 cm, which has been divided into 516 grid points. The number of grid points in each direction is $n_\Psi = 516$, $n_\theta = 64$, and $n_\zeta = 64$, where Ψ, θ, and ζ are the radial, poloidal, and toroidal coordinates, respectively. The resistivity η is determined by Lundquist number $S = (\mu_0 R_0 \nu_A)/\eta$, and the hyper-resistivity is fixed via $\eta_H = 10^{-4}\eta$. The experimental pedestal Lundquist number S varies from 4×10^5 to 1.89×10^7 and is $S = 1.15 \times 10^7$ at the peak gradient position at 3034 ms. In the linear and nonlinear simulations, the Lundquist number is a constant $S = 10^7$, the parallel viscosity is a constant (0.01 in normalized units), and we simulate a toroidal wedge that is 1/5 of the full toroidal angle.

The dependence of the linear ELM growth rate on toroidal mode number is shown in Fig. 1(c) for various assumed values of total plasma current. The 300 kA and 750 kA results in Fig. 1(c) are also based on equilibrium EFITs generated by the Corsica transport code after scaling I_p. The dominant toroidal mode number is $n = 25$ for $I_p = 400$ kA and $n = 30$ for $I_p = 300$ kA, which is consistent with the experimental result in Fig. 1(b). The dominant toroidal mode for $I_p = 750$ kA is $n = 10$, following the trend that lower toroidal mode numbers become dominant when the plasma current increases. Since 1/5 of the torus is simulated, the theoretical results yield an error $\delta n = \pm 2.5$, which is only accurate to $\pm 10\%$–25%. The simulated pressure perturbation of the dominant $n = 25$ Fourier mode (for $I_p = 400$ kA) has been mapped to real space in Fig. 2(a). The bright stripes are the projection of simulated ELM filaments from a synthetic camera diagnostic. The dominant mode also appears at $n = 25$ during the initial linear phase of the nonlinear simulations described next.

Four phases of the ELM crash can be seen in the nonlinear runs. (We note that seven phases of an ELM crash were discussed in Ref. 17.) The normalized rms value of the pressure perturbation $\langle P_{rms} \rangle = \langle \delta P^2 \rangle^{1/2}$, averaged over toroidal angle, is shown in Fig. 3(a). The dotted blue curves separate the four phases of the ELM crash: linear phase-I, nonlinear saturation phase-II, crash phase-III, and L-mode like phase-IV. The structure of the corresponding pressure perturbations is shown in Fig. 3(b). During the linear phase-I, the perturbations increase exponentially. Then, during the nonlinear saturation phase-II,

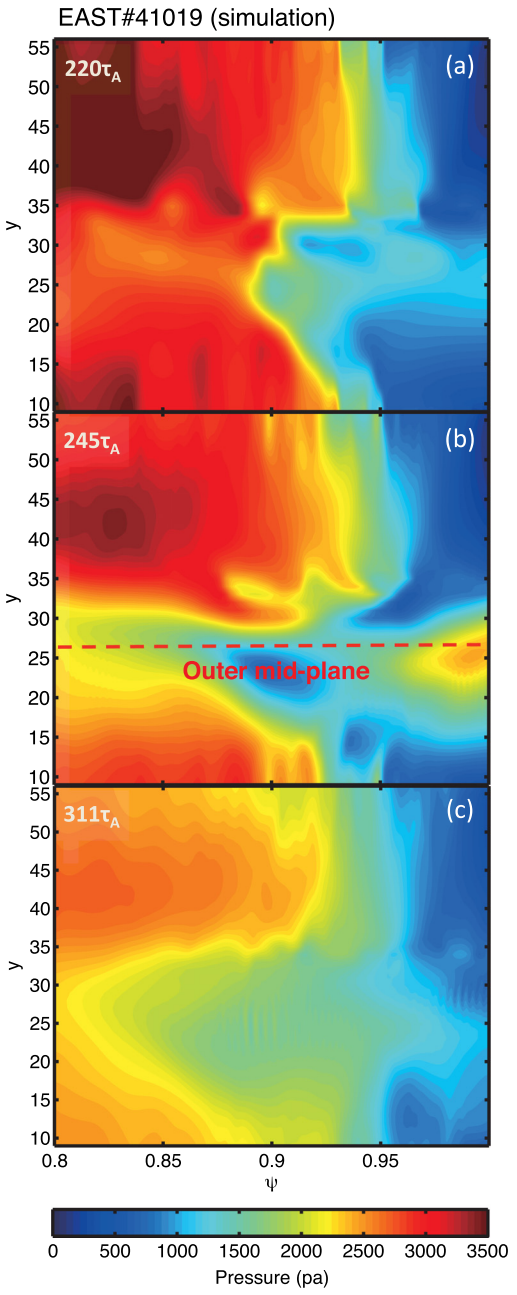

FIG. 4. Simulated axisymmetric pressure profile at different phases of the ELM crash (a) nonlinear saturation phase-II, (b) crash phase-III, and (c) L-mode like phase-IV.

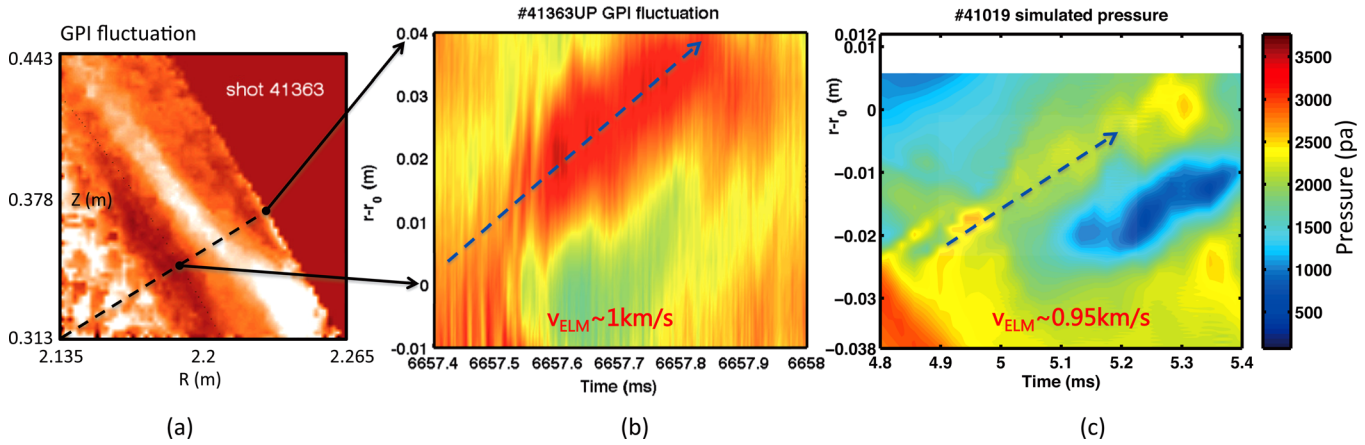

FIG. 5. ELM effluxes measured by the GPI system for discharge #41363: (a) single frame and (b) fluctuations vs. time and radial position along the black dashed line shown in (a). (c) Simulated pressure for discharge #41019 vs. time and radial position along poloidal index $y = 23$, which is inside the GPI window shown in Fig. 2(b).

$\langle P_{rms} \rangle$ drops at the beginning ($t = 203\tau_A$) and then increases rapidly, while the ELM structure appears blurred. During the crash phase-III ($t = [237,\ 255]\tau_A$), $\langle P_{rms} \rangle$ decreases sharply and the structure becomes detached from the pedestal via a magnetic reconnection event. Strong ELM effluxes can be observed during the crash phase. Finally, during the L-mode like phase-IV, $\langle P_{rms} \rangle$ becomes steady and the filamentary structure of the ELM instability is replaced by broadband turbulence. Finally, about 2% of the total energy is ejected as calculated from the nonlinear simulation. The energy loss during the ELM crash in the simulation is defined as

$$\Delta_{ELM}(t) = \frac{\int_{\Psi_{in}}^{\Psi_{out}} d\Psi \oiint J d\theta d\zeta \left(P_0 - \langle P(t) \rangle_\zeta\right)}{\int d\Psi \oiint J d\theta d\zeta P_0}. \quad (1)$$

Here, Ψ_{in} is the inner boundary of the simulation domain and Ψ_{out} is chosen to be the location of the peak pressure gradient. P_0 is equilibrium pressure and J is the Jacobian. This is consistent with the average energy loss measured using the change in stored plasma energy $\Delta W_{MHD}/W_{MHD}$ derived from the EFIT equilibrium reconstruction which is approximately 1.75% during the ELM of shot #41019 just after time = 3034 ms.

The ELM crash starts at the outer midplane and then spreads to the X-point region. Figure 4 shows the evolution of the total pressure profile. The location at $y = 26$ is near the outer mid-plane as shown Fig. 2(b). The collapse of the pressure starts from the outer mid-plane at $t = 203\tau_A$. A mass of ELM efflux crosses the last closed flux surface at $t = 245\tau_A$. Finally, the pressure as a whole decreases to a lower level and becomes steady at $t = 311\tau_A$. The final pressure perturbation profile matches the direction of the measured in-out asymmetry of the power to divertor targets, favoring the outer divertor. This is also consistent with previous measurements of the divertor power asymmetry for EAST.[18] However, this simulation is missing the thermal conduction and sound wave physics that is necessary to fully equilibrate the pressure in the parallel direction.

GPI[19] offers a direct and effective diagnostic to measure the structure and velocity of turbulence in the edge plasma. ELM effluxes were first observed using GPI on EAST discharge #41363 in which parameters are similar to #41019. A typical frame from the GPI diagnostic is shown in Fig. 5(a). The bright stripe shows toroidally averaged ELM effluxes which move from the inside to the outer side in the scrape-off layer. The speed of the ELM effluxes along the direction of the black line in Fig. 5(a) is calculated to be on the order of 1 km/s from the space time plot, shown in Fig. 5(b), which is constructed from a sequence of images. A similar measurement of the speed of ELM effluxes can be made for the nonlinear simulation. We have matched the position of the GPI observing window, the pink rectangle in Fig. 2(b), and the simulation position (poloidal index $y = 23$ is just within the GPI observing window). The speed of the simulated ELM effluxes is also on the order of 1 km/s as shown in Fig. 5(c). In Fig. 5, r_0 is the radius of the separatrix, so the experimental results are measured outside the separatrix, while the simulation results are measured inside the separatrix. Although the agreement may be fortuitous, since the comparison is between data from two different discharges, these results motivate additional research.

In conclusion, experimental analysis of EAST plasma discharge #41019 indicates that the dominant toroidal mode number of ELMs becomes larger for lower current, as predicted in Ref. 11. Nonlinear simulations based on this discharge show four distinct phases during the ELM crash. The simulated mode structure of the ELM instability and the asymmetric deposition of the power fluxes toward the outer divertor are in good agreement with experimental results. The 2% energy loss of the ELM crash and the 1 km/s speed of the ELM effluxes calculated by the simulation are comparable to measurements.

The authors wish to acknowledge Dr. Ben Dud-son and Dr. M. V. Umansky for their contribution to the BOUT++ framework, and Dr. Hong Qin, Dr. Andris Dimits, and Mr. P. W. Xi for useful physics discussions. This work was supported by the National Magnetic Confinement Fusion Program of China (Grant Nos. 2014GB106001, 2014GB106003, 2011GB107001, and 2011GB101000), and the National Natural Science Foundation of China (Grant

Nos. 11021565, 11275234, 11405213, 11405215, 11405217, and 11422546), and was performed under the auspices of the U.S. Department of Energy by Lawrence Livermore National Security, LLC, Lawrence Livermore National Laboratory under Contract No. DE-AC52-07NA27344. LLNL-JRNL-606728.

[1]M. Keilhacker, G. Becker, K. Bernhardi, A. Eberhagen, M. ElShaer, G. FuBmann, O. Gehre, J. Gernhardt, G. V. Gierke, E. Glock, G. Haas, F. Karger, S. Kissel, O. Kluber, K. Kornherr, K. Lackner, G. Lisitano, G. G. Lister, J. Massig, H. M. Mayer, K. McCormick, D. Meisel, E. Meservey, E. R. Muller, H. Murmann, H. Niedermeyer, W. Poschenrieder, H. Rapp, B. Richter, H. Rohr, F. Ryter, F. Schneider, S. Siller, P. Smeulders, F. Soldner, E. Speth, A. Stabler, K. Steinmetz, K.-H. Steuer, Z. Szymanski, G. Venus, O. Vollmer, and F. Wagner, Plasma Phys. Controlled Fusion **26**, 49 (1984).

[2]P. B. Snyder, H. R. Wilson, J. R. Ferron, L. L. Lao, A. W. Leonard, T. H. Osborne, A. D. Turnbull, D. Mossessian, M. Murakami, and X. Q. Xu, Phys. Plasmas **9**, 2037 (2002).

[3]P. B. Snyder, N. Aiba, M. Beurskens, R. J. Groebner, L. D. Horton, A. E. Hubbard, J. W. Hughes, G. T. A. Huysmans, Y. Kamada, A. Kirk, C. Konz, A. W. Leonard, J. Lënnroth, C. F. Maggi, R. Maingi, T. H. Osborne, N. Oyama, A. Pankin, S. Saarelma, G. Saibene, J. L. Terry, H. Urano, and H. R. Wilson, Nucl. Fusion **49**, 085035 (2009).

[4]L. C. Bernard, F. J. Helton, and R. W. Moore, Comput. Phys. Commun. **24**, 377 (1981).

[5]C. R. Sovinec, A. H. Glasser, T. A. Gianakon, D. C. Barnes, R. A. Nebel, S. E. Kruger, D. D. Schnack, S. J. Plimpton, A. Tarditi, M. S. Chu, and NIMROD Team, J. Comput. Phys. **195**, 355 (2004).

[6]G. T. A. Huysmans and O. Czarny, Nucl. Fusion **47**, 659 (2007).

[7]X. Q. Xu, M. V. Umansky, B. Dudson, and P. B. Snyder, Commun. Comput. Phys. **4**, 949 (2008).

[8]P. K. Kaw, E. J. Valeo, and P. H. Rutherford, Phys. Rev. Lett. **43**, 1398 (1979).

[9]X. Q. Xu, B. D. Dudson, P. B. Snyder, M. V. Umansky, H. Wilson, and T. Casper, Nucl. Fusion **51**, 103040 (2011).

[10]X. Q. Xu, B. D. Dudson, P. B. Snyder, M. V. Umansky, and H. Wilson, Phys. Rev. Lett. **105**, 175005 (2010).

[11]Z. X. Liu, T. Y. Xia, X. Q. Xu, X. Gao, J. W. Hughes, S. C. Liu, S. Y. Ding, and J. G. Li, Phys. Plasmas **19**, 102502 (2012).

[12]K. V. Roberts and J. B. Taylor, Phys. Rev. Lett. **8**, 197 (1962).

[13]G. S. Yun, W. Lee, M. J. Choi, J. Lee, H. K. Park, B. Tobias, C. W. Domier, N. C. Luhmann, Jr., A. J. H. Donnè, J. H. Lee, and KSTAR Team, Phys. Rev. Lett. **107**, 045004 (2011).

[14]A. Kirk, H. R. Wilson, G. F. Counsell, R. Akers, E. Arends, S. C. Cowley, J. Dowling, B. Lloyd, M. Price, M. Walsh, and MAST Team, Phys. Rev. Lett. **92**, 245002 (2004).

[15]T. A. Casper, W. H. Meyer, G. L. Jackson, T. C. Luce, A. W. Hyatt, D. A. Humphreys, and F. Turco, Nucl. Fusion **51**, 013001 (2011).

[16]G. Q. Li, Q. L. Ren, J. P. Qian, L. L. Lao, S. Y. Ding, Y. J. Chen, Z. X. Liu, B. Lu, and Q. Zang, Plasma Phys. Controlled Fusion **55**, 125008 (2013).

[17]L. E. Sugiyama and H. R. Strauss, Phys. Plasmas **17**, 062505 (2010).

[18]S. C. Liu, H. Y. Guo, G. S. Xu, X. Gao, S. Z. Zhu, H. Q. Wang, L. Wang, N. Yan, D. S. Wang, P. Liu, M. Jiang, W. Zhang, T. F. Ming, J. F. Chang, S. Y. Ding, H. Xiong, L. M. Shao, Z. W. Wu, G. N. Luo, and EAST Team, Phys. Plasmas **19**, 042505 (2012).

[19]S. C. Liu, L. M. Shao, S. J. Zweben, G. S. Xu, H. Y. Guo, B. Cao, H. Q. Wang, L. Wang, N. Yan, S. B. Xia, W. Zhang, R. Chen, L. Chen, S. Y. Ding, H. Xiong, Y. Zhao, B. N. Wan, X. Z. Gong, and X. Gao, Rev. Sci. Instrum. **83**, 123506 (2012).